

# Characterization of an In-Beam PET Prototype for Proton Therapy With Different Target Compositions

Francesca Attanasi, Nicola Belcari, Sascha Moehrs, *Student Member, IEEE*, Valeria Rosso, Sara Vecchio, *Student Member, IEEE*, G. A. Pablo Cirrone, Giacomo Cuttone, Piero Lojaco, Francesco Romano, Nico Lanconelli, and Alberto Del Guerra, *Senior Member, IEEE*

**Abstract**—At the University of Pisa, the DoPET (Dosimetry with a Positron Emission Tomograph) project has focused on the development and characterization of an *ad hoc*, scalable, dual-head PET prototype for in-beam treatment planning verification of the proton therapy. In this paper we report the first results obtained with our current prototype, consisting of two opposing lutetium yttrium orthosilicate (LYSO) detectors, each one covering an area of  $4.5 \times 4.5 \text{ cm}^2$ . We measured the  $\beta^+$ -activation induced by 62 MeV proton beams at Catania facility (LNS, Catania, Italy) in several plastic phantoms. Experiments were performed to evaluate the possibility to extract accurate phantom geometrical information from the reconstructed PET images.

The PET prototype proved its capability of locating small air cavities in homogeneous PMMA phantoms with a submillimetric accuracy and of distinguishing materials with different  $^{16}\text{O}$  and  $^{12}\text{C}$  content by back mapping phantom geometry through the separation of the isotope contributions. This could be very useful in the clinical practice as a tool to highlight anatomical or physiological organ variations among different treatment sessions and to discriminate different tissue types, thus providing feedbacks for the accuracy of dose deposition.

**Index Terms**—Dose monitoring, positron emission tomography, proton therapy.

## I. INTRODUCTION

**B**ECAUSE of their unique physical and radiobiological properties, radiotherapy with protons and light ions offers several advantages as compared to photons and electrons. Traveling through the patient with minimal lateral diffusion and depositing maximum energy at the end of their range, hadron beams allow highly conformal treatment of deep seated tumors with great accuracy, while delivering minimal doses to surrounding tissues [1], [2].

Conforming the prescribed dose to the target volume can be hampered by the uncertainties arising from approximations of

dose calculation methods in the treatment planning, such as artifacts in the CT and uncertainties in the Hounsfield unit conversion [3]. Although the implementation of safety margins around the tumor and the selection of appropriate portal beams minimize over- or under-shooting effects, discrepancies between planned and actual delivered dose could arise from possible patient misalignments and anatomical or physiological variations among different treatment sessions [4]. This is the reason why a direct verification of radiation field position and particle range would be very desirable for the quality assurance of the treatment.

Multiple studies have shown that Positron Emission Tomography (PET) could fulfill this task adequately, by exploiting the information stored in the reconstructed activity distribution. Since there is no direct correlation between the absorbed dose and activity, delivered dose can be monitored by comparing reconstructed PET images with an activity prediction based on the patient-specific treatment plan as well as on the time course of irradiation and imaging [5]–[10].

The PET method has already turned into a technique of treatment verification for fractionated carbon ion therapy at GSI. The comparison of PET activity distribution predicted on the basis of the planned dose with the measured one has proved to be essential for the routine monitoring of several patients [11]. Similar efforts are now taking place more broadly to demonstrate the clinical utility of the in-beam PET monitoring strategy also in proton therapy. In this respect, we have developed an *ad hoc* dual-head PET prototype to enable application-optimized imaging for the dose monitoring task. The prototype has a modular structure, easy to scale up, geometrically optimized and with the resolution and sensitivity performance required for monitoring purposes at low count rates. At the same time it has to be competitive with commercial state of art clinical PET scanner accuracy.

The prototype performances have been already studied on homogeneous polymethyl methacrylate (PMMA) phantoms by measuring the  $\beta^+$ -activation induced by both 62 MeV proton beams at CATANA facility [12], [13] and low energy carbon beams. In the latter case its performances have been validated against those of the clinically established BASTEI tomograph at GSI [14]. Both experimental investigations have shown the capability of this system for the detection of small range variations along the beam direction, with a submillimetric accuracy.

In this paper, we extend the previous analysis by reporting and discussing the results obtained irradiating several plastic phantoms with 62 MeV protons. By means of two groups of experiments, our proof-of-principle investigation aimed to evaluate

Manuscript received February 11, 2009; revised September 21, 2009; accepted March 21, 2010. Date of current version June 16, 2010. This work was supported in part by the INFN and by the MIUR in the framework of the PRIN2006 program (2006025517 003).

F. Attanasi, N. Belcari, S. Moehrs, V. Rosso, S. Vecchio, and A. Del Guerra are with the Department of Physics, University of Pisa, I-56127 Pisa, Italy and also with INFN Pisa, Largo Bruno Pontecorvo 3, I-56127 Pisa, Italy (e-mail: francesca.attanasi@pi.infn.it).

G. A. P. Cirrone, G. Cuttone, P. Lojaco, and F. Romano are with INFN-LNS, I-95123 Catania, Italy.

N. Lanconelli is with the Department of Physics, University of Bologna, I-40127 Bologna, Italy and also with INFN-Bologna, I-40127 Bologna, Italy.

Color versions of one or more of the figures in this paper are available online at <http://ieeexplore.ieee.org>.

Digital Object Identifier 10.1109/TNS.2010.2048124

the possibility of using information stored in the reconstructed PET images to resolve structures and to distinguish materials of different stoichiometry.

In the first group of experiments, we irradiated three PMMA phantoms containing small air cavities located at different positions along the beam direction. With such kind of experiments, we wanted to evaluate how target  $\beta^+$ -activation dependency on the proton energy can influence the accuracy in detecting and extracting geometrical benchmarks from the activity gradients in the reconstructed PET images. In fact, as the energy of the projectiles diminishes, inelastic nuclear cross sections gradually decrease falling down to zero in the energy range of 15–20 MeV, thus making the extraction of reference points noise-sensitive. The first run of measurements also aimed to the analysis of combined effect of statistical noise and of spatial resolution in extracting activity reference points along depth profiles, throughout the FOV.

In the second group of experiments, by irradiating composite phantoms with plastics characterized by different  $^{16}\text{O}$  and  $^{12}\text{C}$  content, we tried to investigate PET prototype sensitivity in distinguishing materials of different chemical composition by back mapping phantom geometry through the separation of the isotope contributions to the total reconstructed activity.

The paper is organized as follows. Section II describes how experiments were conducted. Section III presents and discusses the results obtained and Section IV draws some conclusions.

## II. MATERIALS AND METHODS

### A. The PET Prototype

A detailed description of the prototype architecture, the calibration procedures and the preliminary experimental results from proton activation study on homogeneous phantoms can be found in [12], [13]. We remind here that the PET prototype is based on two stationary planar heads, consisting of two opposing  $4.5 \times 4.5 \times 1.8 \text{ cm}^3$  lutetium yttrium orthosilicate (LYSO) scintillator matrices,  $21 \times 21$  pixels ( $2 \times 2 \times 18 \text{ mm}^3$  pixel dimensions). A squared position sensitive photomultiplier (Hamamatsu H8500) with an external size of  $5.2 \times 5.2 \times 1.5 \text{ cm}^3$  has been used for measuring the light output. For the position encoding readout, we chose a charge division circuit based on the Symmetric Charge Division (SCD) scheme, reducing the 64 anode signals of each photomultiplier to only 4 acquired per head. The data acquisition is performed using a fast acquisition board previously developed for the small animal PET/ SPECT scanner YAP-(S)PET [15]. The four position signals from each tube are digitized by a system composed of a peak detector plus a peak sensing ADC. The digital data from both detector heads are then transferred to a local PC server via USB connection. In all our post-irradiation measurements at CATANA, the PC server has been placed inside the treatment room, and the acquisitions have been controlled from the beam-line control room by means of a PC client via LAN connection.

Fig. 1 shows the tomographic prototype as positioned on the CATANA beam line: the final brass collimator located upstream

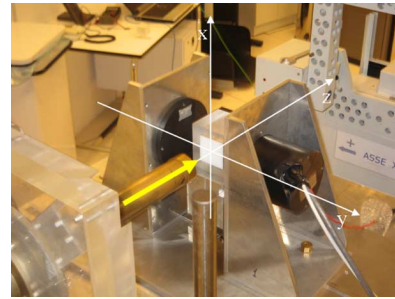


Fig. 1. The installation of the experimental setup at the CATANA beam line. The brass nozzle is visible on the left, the plastic phantom is centered on the beam line and the two detector heads are mounted at the phantom sides, at a distance of 14 cm from each other. The mechanical holder has been built so as to be able to position the detector heads with precision and reproducibility, both in the calibration and in the validation measurements. The chosen coordinate system has been superimposed on the picture.

of the phantom entrance is well recognizable while the two detector heads are mounted at the phantom sides at a distance of 14 cm from each other.

### B. The Experiments on Inhomogeneous Phantoms

Let  $z$  identify the beam direction,  $y$  the direction perpendicular to the entrance surface of the two detector heads and  $x$  the third axis of the coordinate system (see Fig. 1).

In the actual experimental set-up, the PET prototype allows a spatial resolution of 1 mm along  $x$  and  $z$  at the center of the field of view (FOV), but its limited angular acceptance prevents from reaching the same resolution along the  $y$ -axis (currently of  $\approx 7 \text{ mm}$ ) [12], [13]. This is the reason why in our experiments, we did not consider phantoms with inhomogeneities smaller than twice the  $\text{FWHM}_y$  resolution along the  $y$ -axis.

Three phantoms of PMMA ( $5 \times 5 \times 5 \text{ cm}^3$ ) have been constructed, each one containing an air-filled cavity (3 cm thick along the  $y$ -axis and 0.5 cm along the  $z$ -axis). Since we wanted to study the effect of target activation dependency on the proton energy in recovering the position of the air-filled cavity within the FOV, the cavity was located inside the phantoms at different positions along the beam direction, i.e., 5, 10 and 20 mm (see configurations (a), (b) e (c) in Fig. 1).

To investigate the possibility of using information stored in the reconstructed activity to back map phantom geometry in presence of various density values and stoichiometry, two phantoms ( $5 \times 5 \times 5 \text{ cm}^3$ ) were realized assembling differently sized slabs of PMMA ( $\text{C}_5\text{H}_8\text{O}_2$ ) and PE (Polyethylene,  $\text{C}_2\text{H}_4$ ), whose compositions are listed in Table I. A first measurement was done with PMMA and PE inserts (each one 0.5 cm thick along the  $z$ -axis) set side by side and located between the detector heads so that the beam direction was perpendicular to the slabs (see Fig. 2(d)). In the second measurement, two other blocks were stacked one over the other and symmetrized with respect to the central  $yz$  plane (see Fig. 2(e)).

Phantom irradiation modalities were similar to those characterizing the first experiments presented in [12], [13]. Pencil-like proton beams of 62 MeV with an initial energy spread of about 300 keV, shaped by a brass collimator with an aperture diameter of 25 mm, were delivered to the phantoms into the CATANA

TABLE I  
DENSITY AND MAIN COMPOSITION (FRACTION BY WEIGHT) OF THE  
CONSTITUENTS OF THE SLAB PHANTOMS

Material	$\rho$ (gcm <sup>-3</sup> )	H(%)	C(%)	O(%)
PMMA	1.18	8.05	59.99	31.96
* PE	0.93	14.37	85.63	–

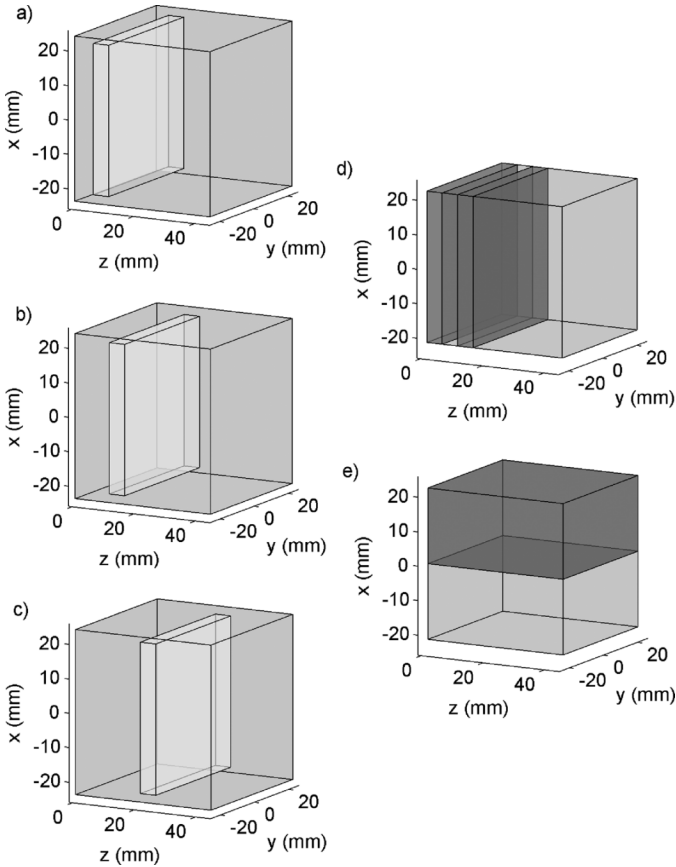


Fig. 2. Phantom layouts. Pictures (a) (b) and (c) display the PMMA phantoms with the cavity at three different  $z$ -positions with respect to the entrance phantom surface. The first one (a) at 5 mm depth, the second one (b) at 10 mm and the last one (c) at 20 mm depth. In pictures (d) and (e) the two geometrical configurations of PE/PMMA phantoms are shown (the light gray indicates PMMA, while the darker one indicates PE). The proton beam impinges to the phantom surfaces from left.

treatment room for eye tumors [16]. During irradiation, all phantoms were positioned at the center of the field of view with the detector heads at a distance of 14 cm.

A parallel plate Markus ion chamber was chosen as reference detector for preliminary absolute dose measurements, while relative measurements of depth dose curves and transverse dose distributions for each proton beam were performed using a silicon diode detector [17] (see Fig. 3).

During each irradiation, a total dose of 30 Gy was delivered in 20–30 s. Data acquisition typically lasted over 20 min starting at the end of irradiation so as to collect good statistics, i.e., up to  $10^5$ – $10^6$  true coincidences. In order to reduce the background noise correlated to the presence of radioactive nuclei ( $^{176}\text{Lu}$ ) in LYSO scintillator, the lower threshold of the acceptance energy window of the acquisition system was set to 350 keV [12], [13].

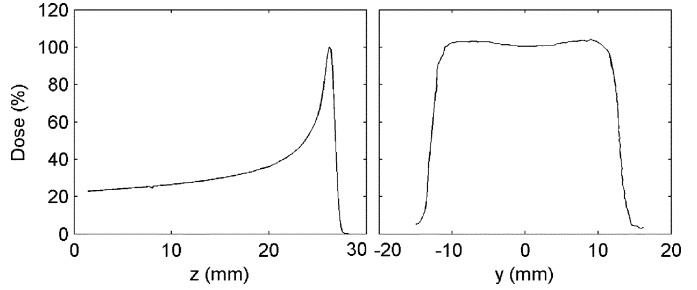


Fig. 3. Experimental depth dose (left) and lateral dose distribution measured with the silicon diode in the final 25 mm diameter circular brass collimator (right).

### C. The Reconstruction Algorithm

We chose an iterative 3D maximum-likelihood expectation maximization algorithm (ML-EM) [18] to reconstruct the distributions of produced positron-emitters in our experiments.

In fact, this unconventional PET application involves count rates which are about one order of magnitude lower than those used in diagnostic nuclear imaging. In addition, the low-statistics activity volumes are also angularly undersampled, thus making essential such a kind of reconstruction.

Here we remind that the  $2\gamma$  coincidences, arising from the annihilation of the emitted positrons, are accumulated as line-of-response (LOR) data in the vector  $\mathbf{p} \in \mathbb{R}^M$  with  $M = 21^4$  LORs, as both, planar detectors had  $21 \times 21$  crystals. The acquisition process is approximated by the linear equation  $\mathbf{A} \cdot \mathbf{u} = \mathbf{p}$ , where  $\mathbf{A} \in \mathbb{R}^{M,N}$  is the system matrix and  $\mathbf{u} \in \mathbb{R}^N$  is the voxelized image, describing the positron-emitter distribution with  $N = 42^3$  voxels of size  $(1.075 \text{ mm})^3$  corresponding to a total image volume of  $(45.15 \text{ mm})^3$ .

The system matrix entries  $A_{m,n}$ , representing the probability that an annihilation event occurring in voxel  $n$  is detected in LOR  $m$ , are calculated offline using the multi-ray method according to [19], which takes the geometry as well as the crystal depth into account. Thus, with the calculated system matrix  $\mathbf{A}$  and the accumulated data  $\mathbf{p}$ , the positron-emitter distribution  $\mathbf{u}$  is reconstructed iteratively by

$$u_i^k = u_i^{k-1} \frac{1}{\sum_{m=1}^M A_{mi} c_m} \sum_{j=1}^M A_{ji} \frac{p_j}{\sum_{n=1}^N A_{jn} u_n^{k-1} + \frac{\lambda_j}{c_j}} \quad (1)$$

with the normalization factors  $c_m$  that contain geometrical as well as crystal efficiency correction factors. They are calculated before the reconstruction according to [20], i.e., the LOR data of an acquired planar source are divided by the data of a planar source that is forward projected with the system model  $\mathbf{A}$ . Finally, the factors  $\lambda_j$  include estimates of the random coincidences and of the LYSO background activity. Instead of subtracting them from the acquired data  $p$  before the reconstruction, they are added to the denominator of (1), e.g., see [21]. For the phantom studies presented here, a small number of ML-EM iterations ( $k = 3$ ) was used to reconstruct the positron-emitter distribution.

#### D. Data Analysis

For all the experiments described in our study, data analysis focused on the possibility of extracting phantom geometrical information from the reconstructed PET images. Since  $\beta^+$ -activation induced by proton beam irradiation depends both on proton energy and target chemical composition, we tried to resolve simple air structures and to distinguish materials of different stoichiometry by means of the activity gradients along the beam direction in the reconstructed images.

In the case of PMMA phantoms with the air cavities, such gradients and their steepness dependence on the cavity position along the beam line was firstly investigated in the central  $xz$  plane. Then, the combined effect of statistical noise and blurring due to the finite spatial resolution of the PET prototype was quantified. To do this, several depth-activity profiles from reconstructed 3D data sets at increasing distances from the central beam axis were extracted. Because of the lack of activity in the air cavity, geometric features for each profile were directly drawn out first by locating the activity minimum around the cavity and then by finding the depths (both at the left and right of the minimum) where the activity assumes the averaged value between the minimum and the adjacent maximum values in the PMMA layer.

In order to recover the phantom geometries also in the case of PMMA/PE phantoms by means of the gradient analysis, we tried to single out the relative amounts of isotopes produced during irradiations and to explore their contributions to the shape of the reconstructed 3D activity distributions. For this purpose, a time analysis on the measured data was performed as already suggested in [10]. For each PET acquisition, the acquired list-mode data were divided into  $s$  data sets of lower statistics following the temporal order. We chose  $s = 5$  so that the number of counts in the  $i$ -th subset was  $C_i \approx 2 \times 10^4 \quad \forall 1 \leq i \leq s$ . For each subset the distribution of positron annihilation points was reconstructed and for each voxel of the FOV (identified by  $(x, y, z)$ ) the data set  $\{n_i(x, y, z)\}_{i=1, \dots, s} \in \mathbb{R}^s$  was fitted by a linear combination of exponential functions:

$$\sum_{j=1}^M N_j^{T_{Irr}}(x, y, z) \cdot \left( e^{-t_i/\tau_j} - e^{-t_{i+1}/\tau_j} \right). \quad (2)$$

Here  $t_i$  and  $t_{i+1}$  are the start and end times of  $i$ -th subset, respectively.  $N_j^{T_{Irr}}(x, y, z)$  are the unknown initial (*i.e.*, at the start of acquisition) amounts of radionuclides of species  $j$  of known mean lifetime  $\tau_j$ , that need to be obtained as best fit parameters. From the knowledge of the initial fraction  $N_j^{T_{Irr}}(x, y, z)$  of each isotope  $j$  we finally recovered the distribution of isotopes,  $N_j^{T_{ot}}(x, y, z)$ , produced during irradiation through the relation:

$$N_j^{T_{Irr}}(x, y, z) = N_j^{T_{ot}}(x, y, z) \cdot \frac{\tau_j}{T_{Irr}} \cdot \left( 1 - e^{-T_{Irr}/\tau_j} \right), \quad (3)$$

where  $T_{Irr}$  is the irradiation duration.

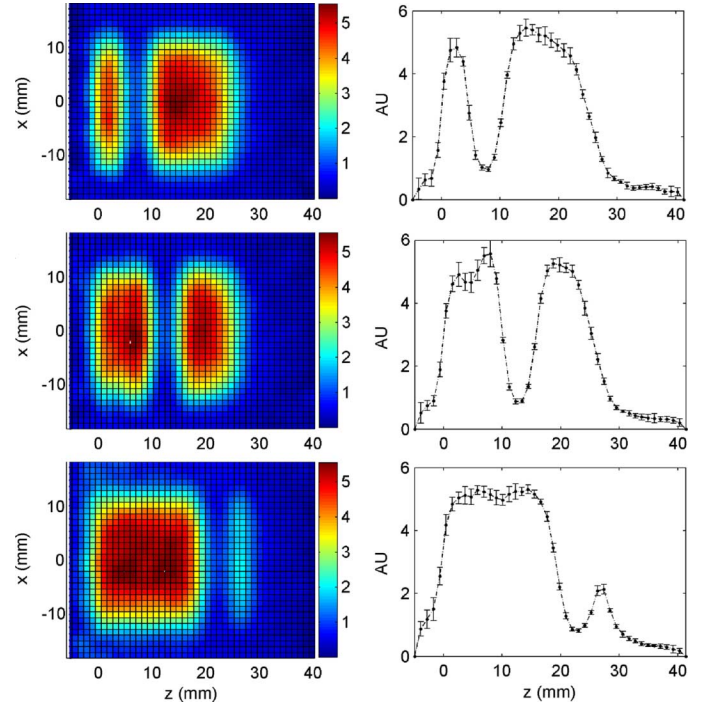


Fig. 4. Left: Reconstructed 2D activity distributions in the central  $xz$  plane. The air cavity (0.5 cm thick along the  $z$ -axis) is at three different positions with respect to the entrance phantom surface (see Fig. 2(a)–(c)). Right: Activation depth profiles through the air-filled cavity, averaged over  $\pm 5$  voxels around the central beam.

On the basis of the chemical composition of our phantoms, the only nuclear reaction channels leading to the production of  $\beta^+$ -radioisotopes are:  $^{12}\text{C}(p, pn)^{11}\text{C}$ ,  $^{16}\text{O}(p, 3p3n)^{11}\text{C}$ ,  $^{16}\text{O}(p, pn)^{15}\text{O}$  and  $^{16}\text{O}(p, 2p2n)^{13}\text{N}$ . We neglected the last one due to its minor contribution in cross section.

### III. RESULTS AND DISCUSSION

Fig. 4 displays the two-dimensional activity distributions in the central  $xz$  plane reconstructed from acquired data during PET investigation on the PMMA phantoms, according to the layouts shown in Fig. 2(a)–(c). Depth-activity profiles, on the right side, represent the projection along the beam direction of the activity averaged over  $\pm 5$  voxels around the central beam axis ( $x = 0$ ). The activity standard deviation ( $\approx 3\%$ ) has been reported as vertical bar on the individual points of the activity profiles.

Due to the lack of the activity in the air-filled cavity, 2D images exhibit high contrast and depth-activity profiles show high peak-to-valley ratios, both for the leading and rising edges next to front and back cavity surfaces. This is evident even in the third geometrical configuration (see Fig. 2(c)) with the cavity located just few millimeters before the Bragg peak: a small amount of activity exceeding the background level is sufficient to recover its position. This confirms that PET resolution for such application does not suffer by proton energy dependency, *i.e.*, does not depend on the location along the penetration depth.

Our attempt to explore the influence of the combined effect of statistical noise and of spatial blurring introduced by the prototype on locating front and back cavity surfaces throughout the

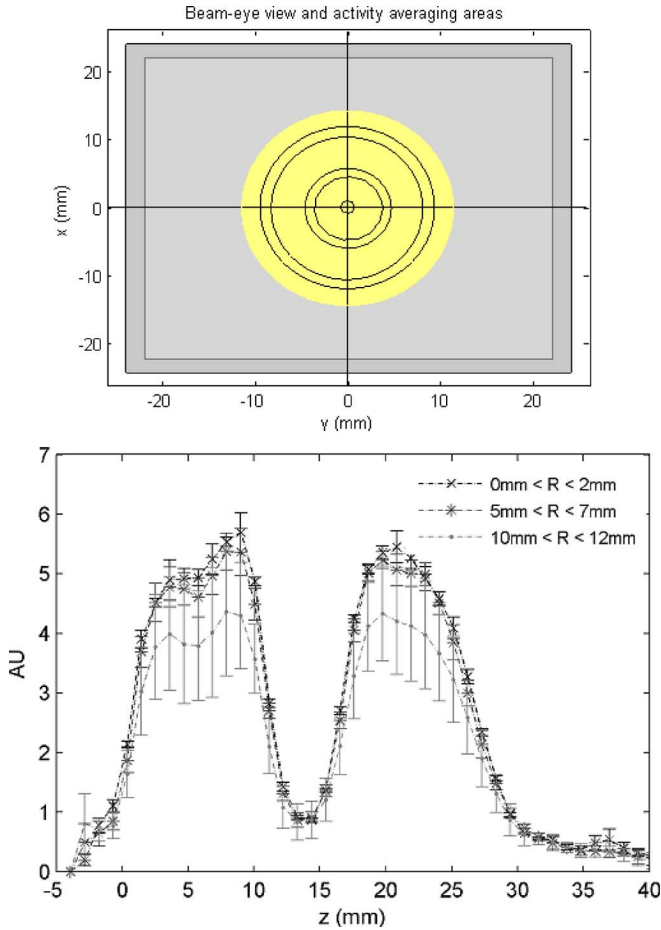


Fig. 5. Three averaged depth-activity profiles extracted from the same 3D data set. The above system of units is based on arbitrary unit values; nevertheless, profiles are not normalized, reflecting the intrinsic difference between them. Lighter gray tones identify the more distant averaging regions (schematically shown in the upper picture) from the central beam axis (black: 0 mm, dark gray: 5 mm and light gray: 10 mm).

FoV, showed how their contribution does not prevent the extraction of reliable benchmarks along the activity gradients also in the more external regions.

An example is given in Fig. 5. It shows a typical comparison of three depth-activity profiles (related to the geometry reported in Fig. 2(b)) extracted from the same 3D reconstructed data set. They represent the projections along the beam axis of the activity averaged within three cylindrical coronas with inner radii of 0 mm, 5 mm and 10 mm, respectively, and outer radii 2 mm greater than the inner ones. The profiles show a great similarity in the high-gradient regions, both in shape and steepness. However, moving from internal to external average domains, both a decreasing of the mean activity and an increasing of the activity standard deviation inside each corona are detectable.

Fig. 6 helps to explain both effects. Since the proton beam has a finite diameter, when the average domain approaches the beam boundary, the reconstructed mean activity becomes diluted and the associated standard deviation rapidly increased. The latter experiences also the effects of the anisotropic spatial resolution of the PET prototype, which introduces a new source of error

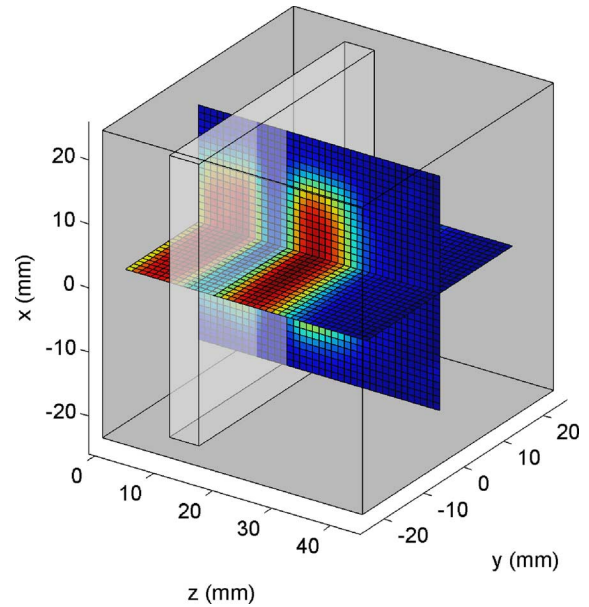


Fig. 6. Two-dimensional distributions of the generated positron emitters in the central  $xz$  and  $yz$  planes inside the phantom (see Fig. 2(b)). There are evidences of the different blurring effects affecting the two planar images, generated by the anisotropic spatial resolution of the PET prototype.

along the polar angle by stretching the activity isosurfaces along the  $y$ -axis, beyond the real beam boundary.

However, this issue was found not to be critical for benchmark extrapolation along the beam direction (like 50% fall-off positions on the activity gradients) needed for cavity localization, whilst it must not be neglected for accurate quantification of the delivered dose. With reference to Fig. 5, for example, the observed variations among the 50% positions extracted along the activity gradients for each depth profile were typically less than one millimeter.

The PET prototype has allowed geometrical information to be inferred from the reconstructed images also in the case of composite phantoms. Fig. 7 shows the PET images of the first irradiated PE/PMMA phantom (see Fig. 2(d)). In the upper left image, the two-dimensional positron emitter distribution in the central  $xz$  plane shows a significant activity contrast between the two materials. Analyzing the averaged depth-activity profile (in the upper right image) two peaks, separated by ten voxels, are detectable. A clearer information about phantom geometry arises from the separation of isotope contributions within the total activity. In particular, the extrapolation of the activity edges from the spatial  $^{15}\text{O}$  distribution shows how PMMA alternates with the PE slabs.

The same considerations can be extended also to the case of the phantom with the PE and PMMA blocks arranged as shown in Fig. 2(e). The corresponding PET images are reported in Fig. 8. In the upper left image, the two-dimensional positron emitter distribution in the central  $xz$  plane shows an increased activity in the PMMA region since the short-lived isotope  $^{15}\text{O}$  is detected additionally to  $^{11}\text{C}$ , as indicated by the separation of isotope contributions displayed in the lower images. Furthermore, analyzing the two averaged depth-activity profiles (in the right upper image of Fig. 8) we also observe a difference in the

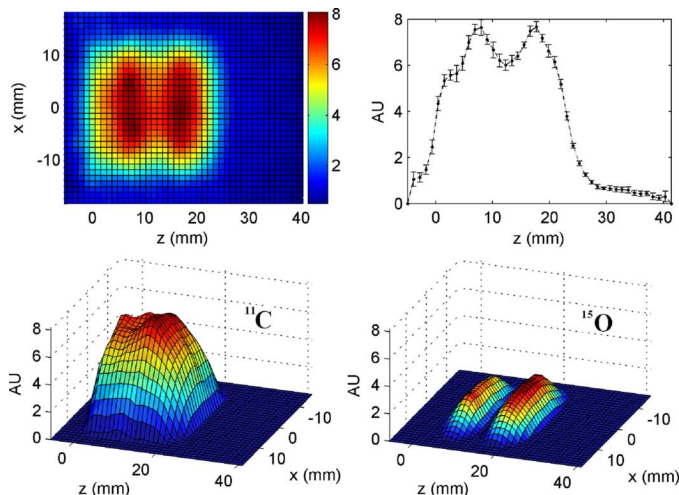


Fig. 7. Reconstructed PET images for the PE/PMMA phantom (configuration Fig. 2(d)). Top Left: Reconstructed 2D activity distribution in the central  $xz$  plane. Top right: Depth profile averaged over a circular cross section with a diameter of 10 mm centered around the central beam axis. Bottom: Spatial distribution of  $^{11}\text{C}$  (left) and  $^{15}\text{O}$  (right) isotopes produced during irradiation in each pixel of the central  $xz$  plane.

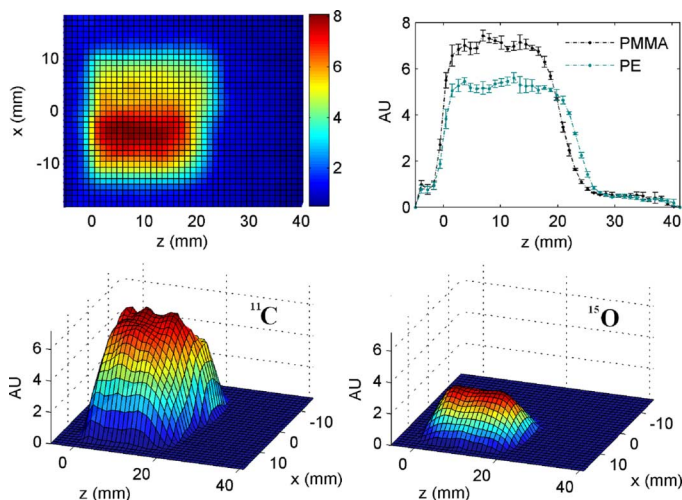


Fig. 8. Reconstructed PET images for the PE/PMMA phantom (configuration Fig. 2(e)). Top Left: Reconstructed 2D activity distribution in the central  $xz$  plane. Top right: Depth-activity profiles extracted from each material. The reported vertical error bars along the depth profiles represent the experimental standard deviation ( $\pm\sigma$ ), within a circular sector in each material. Bottom: Spatial distributions of  $^{11}\text{C}$  (left) and  $^{15}\text{O}$  (right) isotopes produced during irradiation in each pixel of the central slice.

proton practical range. This difference can be explained by the difference in density between PE and PMMA.

#### IV. CONCLUSIONS AND FUTURE WORK

We presented the results obtained with an *ad hoc* dual head PET prototype after irradiation of different phantoms with 62 MeV proton beams. Our study represents a proof-of-principle investigation into the possibility of using information stored in the reconstructed PET images to resolve structures of different stoichiometry within the irradiated volume.

By irradiating several PMMA phantoms, each one containing an air-filled cavity at different positions along the  $z$ -axis, we observed that strong activity gradients are present in the PET im-

ages along the whole beam line, up to few millimeters before the Bragg peak. They provide reliable benchmarks to obtain cavity positioning, even in the most critical configuration, where nuclear cross sections fall down to zero rapidly. Exploring the influence of the combined effect of the statistical noise and of the spatial resolution on locating the air filled cavity throughout the FoV, we observed that their effect does not preclude the possibility to extract reliable benchmarks along the beam line also in the most external regions, where the effect of anisotropic PET resolution is not negligible.

The experiments with inhomogeneous phantoms demonstrated the sensitivity of the PET method in distinguishing material of different chemical composition. By back mapping phantom geometries through the separation of the isotope contributions we observed how a data acquisition soon after the end of irradiation allow structures of different stoichiometry to be resolved at least qualitatively. Quantitative analysis are now under investigation and will be reported in a separated paper.

In conclusion, these capabilities may reasonably prove to be useful in the clinical practice as a tool to highlight anatomic variations (for example, due to internal organ movements) or discrepancies in patient positioning between two treatment sessions with reference to the expected activity distribution based on planning CT. However, the application of such potential millimeter precision to real clinical cases requires a detailed knowledge of the tissue stoichiometry and of the details of all reaction channels leading to the production of positron emitters. Future experiments in more realistic phantoms with a prototype with a greater solid angle coverage are expected to improve and validate the proposed application.

#### REFERENCES

- [1] D. W. Miller, "A review of proton beam radiation therapy," *Med. Phys.*, vol. 22, pp. 1943–1954, 1995.
- [2] U. Amaldi and G. Kraft, "Radiotherapy with beams of carbon ions," *Rep. Prog. Phys.*, vol. 68, pp. 1861–1882, 2005.
- [3] B. Schaffner and E. Pedroni, "The precision of proton range calculations in proton radiotherapy treatment planning: Experimental verification of the relation between CT-HU and proton stopping power," *Phys. Med. Biol.*, vol. 43, pp. 1579–1592, 1998.
- [4] M. Engelsman and H. M. Kooy, "Target volume dose considerations in proton beam treatment planning for lung tumors," *Med. Phys.*, vol. 32, no. 12, pp. 3549–3557, 2005.
- [5] W. Enghardt *et al.*, "Positron emission tomography for quality assurance of cancer therapy with light ion beams," *Nucl. Phys. A*, vol. 654, pp. 1047c–1050c, 1999.
- [6] F. Pönisch *et al.*, "The description of positron emitter production and PET imaging during carbon ion therapy," *Phys. Med. Biol.*, vol. 49, pp. 5217–5232, 2004.
- [7] K. Parodi and W. Enghardt, "Potential application of PET in quality assurance of proton therapy," *Phys. Med.*, vol. 45, no. 11, pp. N151–6, 2000.
- [8] K. Parodi *et al.*, "Clinical CT-based calculations of dose and positron emitter distributions in proton therapy using the FLUKA Monte Carlo code," *Phys. Med. Biol.*, vol. 52, no. 12, pp. 3369–3387, 2007.
- [9] K. Parodi and T. Bortfeld, "A filtering approach based on Gaussian-powerlaw convolutions for local PET verification of proton therapy," *Phys. Med. Biol.*, vol. 51, no. 8, pp. 1991–2009, 2006.
- [10] F. Attanasi *et al.*, "Experimental validation of the filtering approach for dose monitoring in proton therapy at low energy," *Phys. Med.*, vol. 24, pp. 102–106, 2008.
- [11] W. Enghardt *et al.*, "Charged hadron tumour therapy monitoring by means of PET," *Nucl. Instrum. Methods Phys. Res. A*, vol. A525, pp. 284–288, 2004.
- [12] S. Vecchio *et al.*, "A PET prototype for in-beam monitoring of proton therapy," *IEEE Trans. Nucl. Sci.*, vol. 56, no. 1, pp. NS24–362, Feb. 2009.

- [13] F. Attanasi *et al.*, "Preliminary results of an in-beam PET prototype for proton therapy," *Nucl. Instrum. Methods Phys., Res. A*, vol. A591, pp. 296–299, 2008.
- [14] F. Attanasi *et al.*, "Comparison of two dedicated in beam PET systems via simultaneous imaging of  $^{12}\text{C}$ -induced  $\beta^+$ -activity," *Phys. Med. Biol.*, vol. 54, pp. N29–N35, 2009.
- [15] A. Del Guerra *et al.*, "Performance evaluation of the fully engineered YAP-(S)PET scanner for small animal imaging," *IEEE Trans. Nucl. Sci.*, vol. 53, no. 3, pp. 1078–1083, Jun. 2006.
- [16] G. A. P. Cirrone *et al.*, "A 62-MeV proton beam for the treatment of Ocular Melanoma at Laboratori Nazionali del Sud-INFN," *IEEE Trans. Nucl. Sci.*, vol. 51, no. 3, pp. 860–865, Jun. 2004.
- [17] L. Raffaele *et al.*, "Proton beam dosimetry for the CATANA project," *Phys. Med.*, vol. XVII (Suppl. 3), pp. 35–40, 2001.
- [18] L. Shepp and Y. Vardi, "Maximum likelihood reconstruction for emission tomography," *IEEE Trans. Med. Imag.*, vol. 1, pp. 113–122, 1982.
- [19] S. Moehrs *et al.*, "Multi-Ray based system matrix generation for 3D PET reconstruction," *Phys. Med. Biol.*, vol. 53, no. 23, pp. 6925–6945, 2008.
- [20] W. Wang, Z. Hu, and D. Gagnon, "A new component approach to efficiency normalization for 3D PET," *IEEE Trans. Nucl. Sci.*, vol. 54, no. 1, pp. 92–99, Feb. 2007.
- [21] D. J. Kadmas, "LOR-OSEM: Statistical PET reconstruction from raw line-of-response histograms," *Phys. Med. Biol.*, vol. 49, no. 20, pp. 4731–4744, 2004.